Tunable High-Temperature Afterglow through Recombination of Thermally Released Excitons

Ping Jiang, Bingbing Ding*, Jiayi Yao, Lei Zhou, Zhenyi He, Zizhao Huang, Chenjia Yin, He Tian, Xiang Ma*

Key Laboratory for Advanced Materials and Feringa Nobel Prize Scientist Joint Research Center, Frontiers Science Center for Materiobiology and Dynamic Chemistry, Institute of Fine Chemicals, School of Chemistry and Molecular Engineering, East China University of Science and Technology, Meilong Road 130, Shanghai 200237, P. R. China

Abstract

Developing smart materials with tunable high-temperature afterglow (HTA) luminescence remains a formidable challenge. This study presents a metal-free doping system using boric acid as matrix and polycyclic aromatic hydrocarbons as dopants. This composition achieves dynamically tunable afterglow combining a bright blue HTA lasting for over ten seconds even at 150℃ and an ultra-long yellow room-temperature phosphorescence (RTP) below 110℃. The observed HTA is attributed to the electron-hole recombination within the dopant molecules. Heating stimuli release the trapped electrons from oxygen vacancies formed by boric acid. The planarity of dopants is investigated playing a pivotal role in modulating Dexter electron transfer (ET) for capturing released electrons by dopants and thereby affecting the overall performance of tunable HTA. This work provides an efficient and universal doping strategy to engineer tunable HTA through the synergistic action of thermally releasing electrons, Dexter ET and electron-hole recombination.

Introduction

The ultralong afterglow luminescence after ceasing excitation source has caught wide attention in bioimaging[1-3], information encryption[4-7], and other attractive areas[8-14]. While numerous ultralong afterglow materials have been successfully synthesized through strategies like H-aggregation[15-17], host-

https://doi.org/10.26434/chemrxiv-2024-vd18g ORCID: https://orcid.org/0000-0002-8679-4491 Content not peer-reviewed by ChemRxiv. License: CC BY-NC-ND 4.0

guest doping[18-22], polymerization[23-26], and others[27-36], the developments of smart materials with dynamic tunable afterglow, especially those resilient to high temperature, are still challenging. The dynamic high-temperature afterglow (HTA) materials could respond to external stimuli and manifest varying luminescence behaviors, which offer a broader practical application such as in photonic communication[37]. Both thermally activation delayed fluorescence (TADF) and room-temperature phosphorescence (RTP) rely on triplet states (**Figure 1a**), exhibiting prolonged lifetime ranging from microseconds to seconds. Therefore, the integration of dual emission based on TADF and RTP was considered one of the most convenient strategies to obtain dynamic afterglow materials in the past works[38-43]. Traditional dynamic dual ultralong afterglow requires two prerequisites: 1) Sufficiently long-lived triplet states to support persistent luminescence. 2) Multiple exciton decay pathways to enable multi-channel emission at differing temperatures. However, triplet states tend to deactivate at elevated temperatures, rendering TADF and RTP emissions difficult to maintain[44-46]. This results in a restricted temperature range for tunable HTA, seriously impeding the realization of materials with a truly broad and dynamic temperature-dependent tunability in their afterglow properties.

Thermoluminescence (TL), commonly found in inorganic system, arises from the recombination of thermally released electrons with ionization centers[47;48]. Generally, TL materials contain a specific concentration of both luminescent centers and traps[49]. These traps are locally anomalous structures formed by the defects or impurities within a crystal. Upon materials exposure to light or ray particles radiation, free electrons are generated and diffuse towards defects and impurities and thus be trapped[41]. When the materials are heated up, the captured electrons receive energy through thermal lattice vibrations and escape from these traps. Subsequently, the rediffused free electrons recombine with free holes, accompanying TL emission. It was reported that boric acid (BA), following heat treatment, exhibited TL emission at high temperature due to the presence of oxygen vacancies[50;51]. The heated **BA** was regarded as a good energy donor to realize the dynamic HTA through the Dexter electrons transfer (ET).

https://doi.org/10.26434/chemrxiv-2024-vd18g **ORCID:** https://orcid.org/0000-0002-8679-4491 Content not peer-reviewed by ChemRxiv. **License:** CC BY-NC-ND 4.0

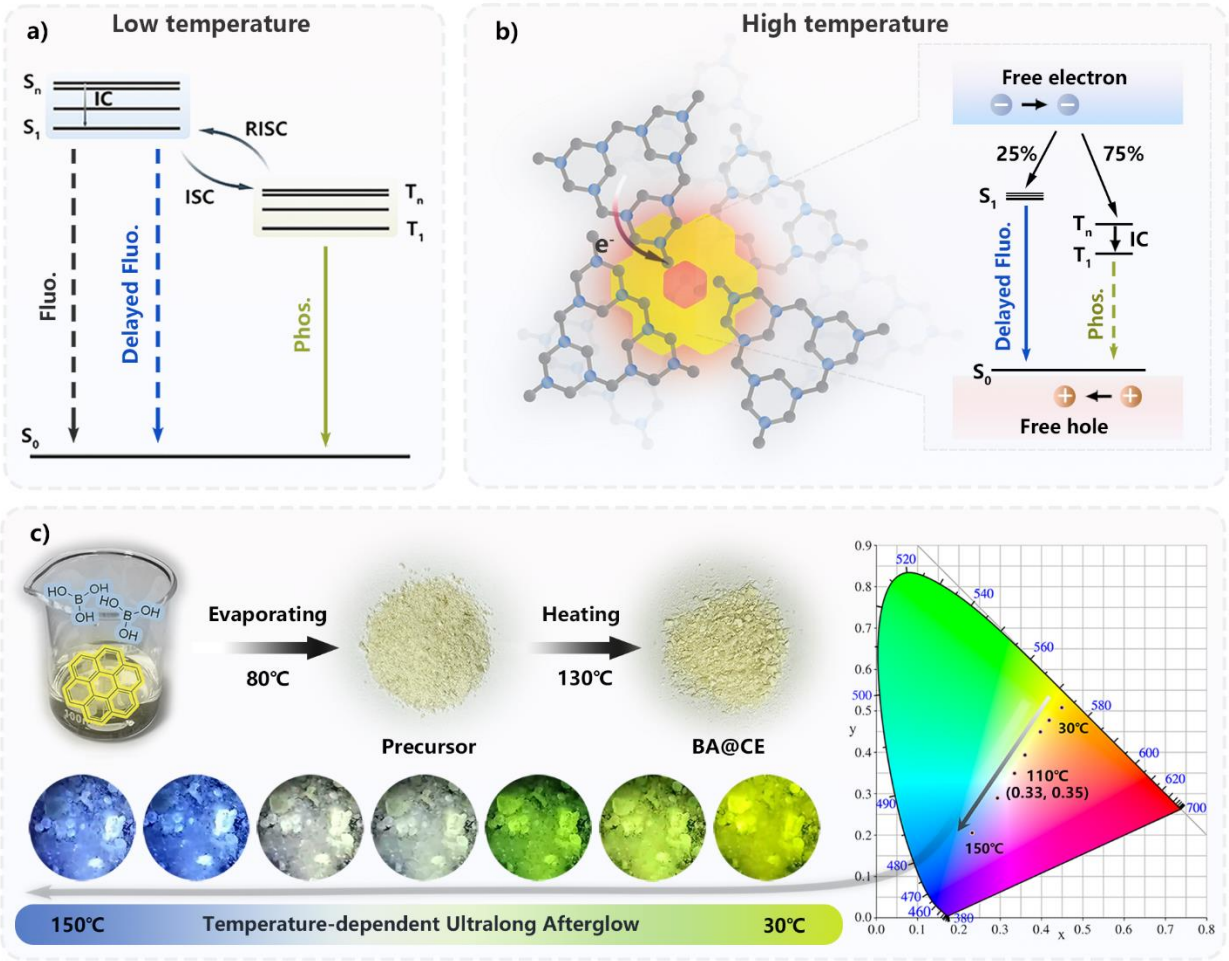

Figure 1. Schematic diagram of tunable HTA emission and material preparation. (a) Simplified Jablonski diagram showing RTP at lower temperature, IC: internal conversion; ISC: intersystem crossing; RISC: reverse intersystem crossing; (b) Schematic diagram of HTA generated through recombination of thermally released free electrons; (c) Preparation method of **BA@CE**; photographs of temperature-dependent ultralong afterglow, and corresponding CIE coordination.

Herein, the coronene (**CE**) was strategically selected as the acceptor of the thermally released free electrons within **BA** matrix for giving efficient HTA. After doped into **BA** matrix, the **CE** molecules served as the recombination center of the accepted electrons and residual holes, yielding 25% singlet and 75% triplet excitons which, respectively, contribute to ultralong delayed fluorescence and phosphorescence (**Figure 1b**). Remarkably, despite the typically rapid decay of triplets at elevated

https://doi.org/10.26434/chemrxiv-2024-vd18g ORCID: https://orcid.org/0000-0002-8679-4491 Content not peer-reviewed by ChemRxiv. License: CC BY-NC-ND 4.0

temperatures, a blue HTA persisted even at temperature as high as 150℃ due to the presence of excited singlets and long-lived trapped electrons. At temperature below 110℃, the trapped electrons hardly escape to produce either TL or DF emissions. However, benefiting from BA's rigid microenvironment created upon heating and dehydration, yellow phosphorescence from CE became dominant, following conventional photophysical pathways with intersystem crossing (ISC) as a pivotal step (**Figure 1a**). Rigidity-induced RTP and thermally released electrons-triggered delayed fluorescence conjointly constitute the temperature-tunable ultralong afterglow, of which white afterglow (0.33, 0.35) could be achieved at 110℃ (**Figure 1c**). To further explore the influence factors of HTA efficiency and temperature-responsive tunability, a series of polycyclic aromatic hydrocarbons (PAHs) varying in planarity were employed. It was observed that dopants with increased planarity facilitate closer proximity to the matrix, thereby promoting HTA via more efficient Dexter electron transfer (ET) processes. This research presents a metal-free doping strategy that universally enables tunable HTA by effectively harnessing the recombination of thermally released free electrons.

Results and discussion

Preparation and structural characterization of doping materials. The preparation procedure of **BA@CE** is showed in **Figure 1c.** A **BA@CE** precursor powder was obtained by gentle evaporation of a water/1,4-dioxane (1/1, v/v) solvent containing dopant/**BA** (0.5 wt%) to ensure an even distribution of dopants throughout the mixture. The resulting **BA@CE** precursor powder was then heated under 130°C at air atmosphere for 20 minutes to facilitate dehydration and yield the final product. During this dehydration process, BA undergoes two distinct phase transformations: first from its triclinic structure to orthorhombic metaboric acid, followed by conversion to vitreous boron oxide[50;51]. This process inherently creates oxygen vacancies and a rigid microenvironment within the material. The thermogravimetric analysis (TGA) of **BA**, **CE** and **BA@CE** were tested in **Figure 2e** to analyze the dehydration behavior and thermal stability. The TGA curve of **BA** displayed a significant weight loss above 100°C, with a

https://doi.org/10.26434/chemrxiv-2024-vd18g **ORCID:** https://orcid.org/0000-0002-8679-4491 Content not peer-reviewed by ChemRxiv. **License:** CC BY-NC-ND 4.0

maximum weight loss of 43.7%, signifying the complete dehydration transition from **BA** to boron oxide. In contrast, TGA results for **CE** showcased excellent thermal stability within the temperature range up to 130°C, evidencing that **CE** did not decompose during the heat treatment process.

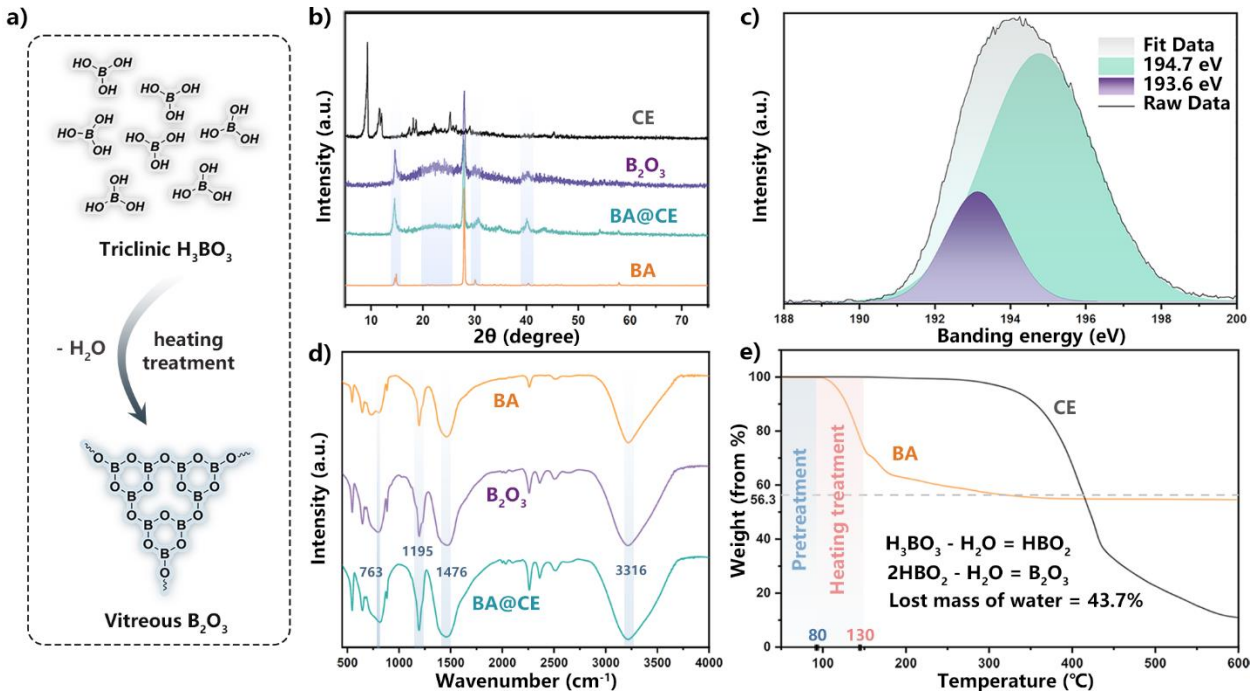

Figure 2. Structural characterization of BA@CE. (a) Dehydration process of **BA** under heating treatment; (b) XRD of **BA**, **B_2O_3**, **CE**, and 0.5 wt% **BA@CE**; (c) XPS of 0.5 wt% **BA@CE**; (d) FT-IR of **BA**, **B_2O_3**, and 0.5 wt% **BA@CE**; (e) TGA of **BA** and **CE**.

The composite structure of bicomponent system was analyzed by X-Ray powder diffraction (XRD), X-ray photoelectron spectroscopy (XPS), and Fourier transform infrared spectroscopy (FT-IR). **Figure 2a** demonstrating the dehydration process of **BA** after the heating treatment. The XRD analysis of **CE, B_2O_3**, **BA@CE**, and **BA** were collected in **Figure 2b**. **BA** showed a sharp diffraction peaks, indicating the crystalline structure. The strong diffraction peaks of **CE** are invisible after doped into the matrix **BA**. Besides, **BA@CE** exhibited similar feature with **B_2O_3**, a broaden peak in 15°, 25°, 28° and 40°, illustrating the decrease of crystallinity. These results were consistent with the XPS analysis (**Figure 2c**).

https://doi.org/10.26434/chemrxiv-2024-vd18g **ORCID:** https://orcid.org/0000-0002-8679-4491 Content not peer-reviewed by ChemRxiv. **License:** CC BY-NC-ND 4.0

The high-resolution B 1s spectra of **BA@CE** can be fitted to two bands centered at 193.6 eV, and 194.7 eV, which belonged to the B_2O_3 and B-O respectively. In **Figure 2d**, FT-IR characterized peaks of **BA**, locating at 763, 1195, 1476, and 3316 cm^{-1}, were corresponding to stretching vibrations of B–O–B bonds, plane B–O–H bending, stretching vibrations of B–O and –OH, respectively. Results above demonstrated the dehydration process after heating process.

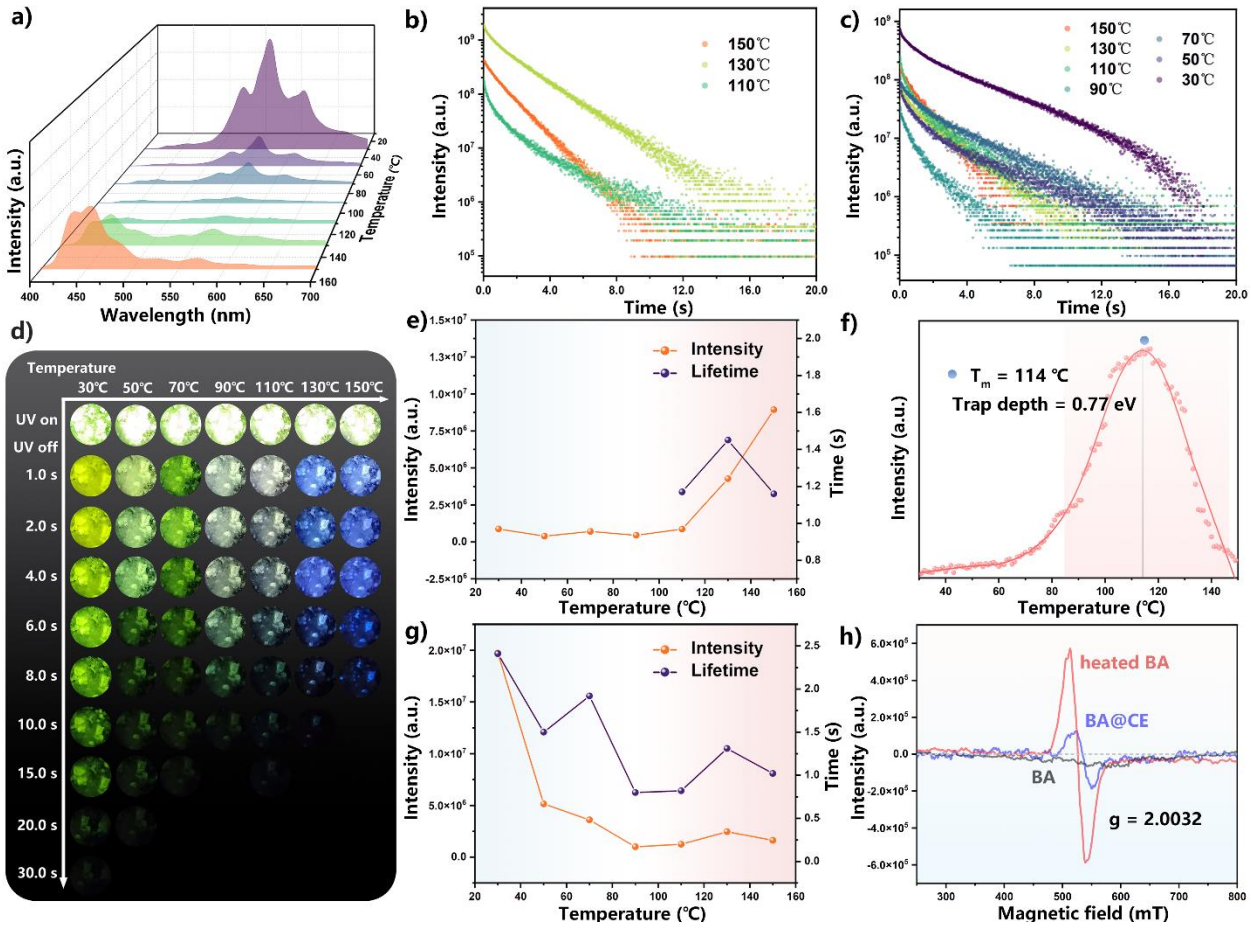

Figure 3. Photophysical properties of materials. (a) Delayed emission spectra of **BA@CE** (0.5 wt%); Decay curves of delayed emissions at 450 nm (b) and 560 nm (c); (d) Afterglow images of 0.5 wt% **BA@CE** after 365 nm UV irradiation; Temperature-dependent emission intensity and lifetime at 450 nm (e) and 560 nm (g) of 0.5 wt% **BA@CE**; (f) TL glow curves of heated **BA**; (h) ESR of **BA**, heated **BA**, and 0.5 wt% **BA@CE** after 365 nm UV irradiation.

https://doi.org/10.26434/chemrxiv-2024-vd18g **ORCID:** https://orcid.org/0000-0002-8679-4491 Content not peer-reviewed by ChemRxiv. **License:** CC BY-NC-ND 4.0

The photophysical properties of BA@CE. Among the myriad of luminophores in PAHs, the **CE** was selected as a representative to be the electron acceptor due to its high electron mobility and excellent optical properties. The delayed emission spectra and relevant lifetime decay curves of 0.5 wt% **BA@CE** at different temperature were tested and detailed in **Figure 3a-c**. The delayed emission peaks for **BA@CE**, observed at around 560 nm, were found to be in alignment with the phosphorescence emission peaks of a **CE** solution at 77K (**Figure S1a**). Similarly, the delayed emission at 450 nm for **BA@CE** was consistent with the fluorescence emission of the **CE** solution (**Figure S1b**). The emission's multi-peak pattern is ascribed to the vibrational energy levels inherent in PAHs[52]. These correspondences confirm that the dual delayed emission phenomenon originates from the dopant itself. **Table S1** summarized the delayed emission lifetimes for 0.5 wt% **BA@CE** across various temperature. The longest lifetime for delayed fluorescence was 1.95 s and the longest lifetime for phosphorescence extended to 2.41 s. The afterglow images of **BA@CE** (**Figure 3d**) delineate a shift in the afterglow color from the yellow of phosphorescence at 30℃ to the blue of delayed fluorescence at 150℃. At 110℃, the system exhibits a distinctive white light afterglow, with the Commission Internationale de l'Eclairage (CIE) coordinates (**Figure 1c**) precisely measured at (0.33, 0.35). Upon surpassing a temperature threshold of 110°C, there is a marked escalation in the delayed emission observed at 450 nm (**Figure 3e**). This enhancement is attributed to the CE's role as an electron acceptor, capturing thermally released electrons. Because the rigidity environment formed by heated **BA** suppressed radiative energy loss by molecular vibration, a strong RTP emission from was originated of dopants itself. The phosphorescence intensity of **BA@CE** exhibited a decline with an increase in temperature from 30℃ to 110℃. Notably, an anomalous enhancement occurred upon reaching 130℃ from 110℃ (**Figure 3g**). This observation suggests a process of thermally induced electron release. The behavior of different concentrations of **CE** (1.0 wt% and 5.0 wt%) in doping systems was also discussed, as shown in **Figures S3** and **S4**, which display a tendency analogous to that of 0.5 wt% **BA@CE**.

https://doi.org/10.26434/chemrxiv-2024-vd18g **ORCID:** https://orcid.org/0000-0002-8679-4491 Content not peer-reviewed by ChemRxiv. **License:** CC BY-NC-ND 4.0

The intrinsic mechanism of HTA. The luminescence behaviors of heated **BA** across various temperatures were studied firstly. Initially, the temperature-dependent delayed emission spectra of heated **BA** were examined. Notably, under 360 nm excitation, a broad peak at 495 nm was observed (**Figure S11a**), which was attributed to the TL emission. A significant surge in intensity was detected at a pivotal temperature of 110°C, which was consistent with the delayed emission trend at 450 nm for **BA@CE**. TL glow curve in **Figure 3g** exhibited a maximum peak temperature (T_m) at 114°C, which indicated the presence of trapped electrons by structural defects. The trap depth was estimated to be 0.77 eV below the conduction band, calculated using the formula $E(eV) = T_m(K)/500$. Additionally, the ESR spectrum of heated **BA** and **BA@CE** were also displayed in **Figure 3h.** The central resonance field corresponds to g-value of 2.0032, which falls within the range typically attributed to oxygen vacancy. The TL observed in heated **BA** is attributed to the recombination of thermally released electrons originating from oxygen vacancies[53]. Upon the incorporation of **CE** into **BA**, the generated TL-like HTA emission is also hypothesized to occur through a similar recombination mechanism involving thermally released electrons from oxygen vacancies. However, the presence of **CE** introduces a key difference in the system. The addition of **CE** introduces a favorable recombination center within the material. The provision of an alternative recombination site by **CE** likely alters the energy levels and pathways available for electron-hole recombination, thus influencing the emission characteristics, including its wavelength.

Figure 4a illustrates the detailed photophysical processes of HTA observed in **BA@CE**. The traps of matrix were built up in crystallographic vacancies-induced defects (i). Upon UV exposure, excited electrons are diffused throughout crystalline lattice and attracted to electron traps, leaving behind holes (ii). These trapped electrons are immobilized until external heat provides enough energy for them to escape and would recombine with holes, emitting TL (iii). However, the introduced dopant could add new charge recombination centra and generate the HTA instead of TL with different wavelength through Dexter ET of escaped electrons (iv). A model in **Figure 4b** explains the afterglow mechanism at high temperatures, where electrons of matrix absorb light, moving to the conduction band (CB) and creating

https://doi.org/10.26434/chemrxiv-2024-vd18g **ORCID:** https://orcid.org/0000-0002-8679-4491 Content not peer-reviewed by ChemRxiv. **License:** CC BY-NC-ND 4.0

electron and hole carriers. The electrons, captured by oxygen vacancy traps, can be released with additional energy, such as heat. When luminophores act as electron acceptors, Dexter ET can occur at the matrix-dopant interface, with the efficiency potentially influenced by the intermolecular distance between donor and acceptor. Electrons can move from the CB to the dopant's lowest unoccupied molecular orbital (LUMO) and recombine with holes in the highest occupied molecular orbital (HOMO), forming singlet and triplet states with probabilities of 25% and 75%, respectively[54-56].

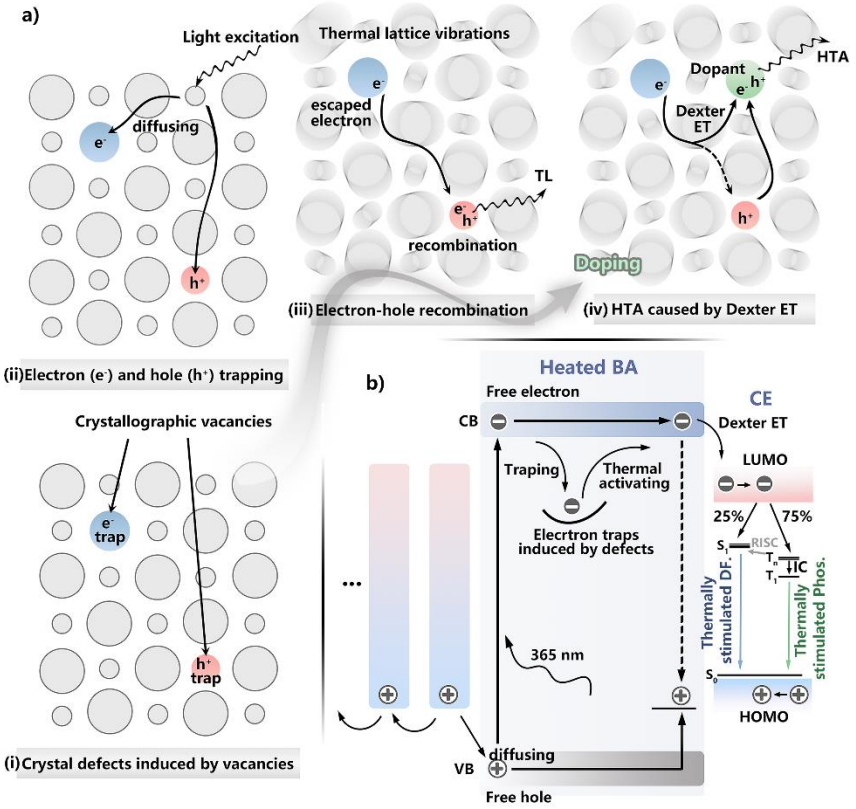

Figure 4. Schematic diagram of charge trapping and releasing. (a) Mechanism of HTA in the **BA@CE** materials. (b) A crystalline lattice (i), depicting common lattice defects induced by vacancies; Trapping (ii) and escaping (iii) of an electron-hole pair in the crystal; (iv) HTA caused by Dexter ET after doping in the matrix.

https://doi.org/10.26434/chemrxiv-2024-vd18g ORCID: https://orcid.org/0000-0002-8679-4491 Content not peer-reviewed by ChemRxiv. License: CC BY-NC-ND 4.0

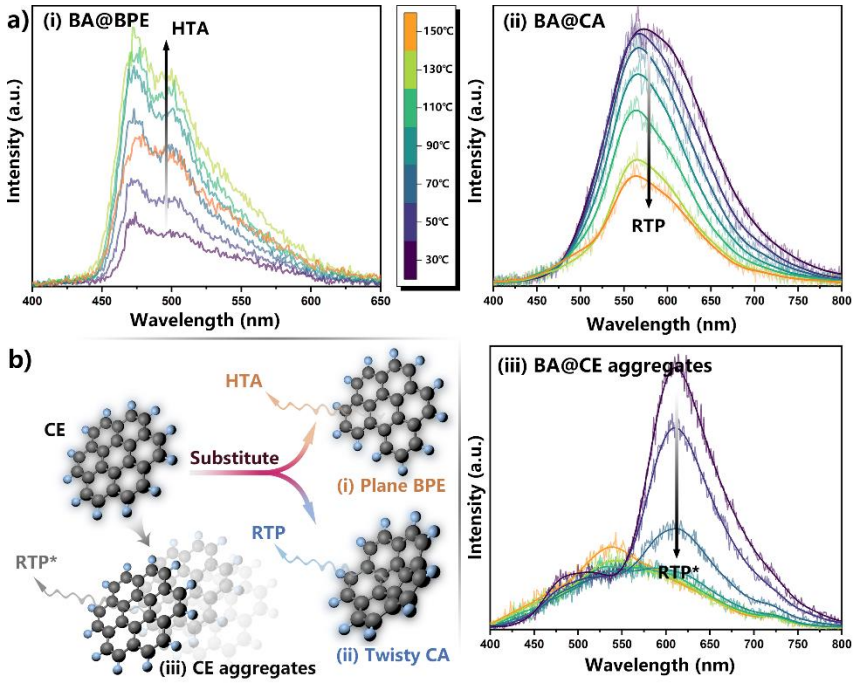

Figure 5. Photophysical properties of contrasting agents. (a) Delayed emission spectra of 0.5 wt% **BA@BPE** (i), 0.5 wt% **BA@CA** (ii), and 10 wt% **BA@CE** (iii) under different temperature; (b) Dopant substitutes of plane **BPE**, twisty **CA** and **CE** aggregates.

As discussed above, the distance between dopants and matrix is likely a crucial determinant of HTA, as it significantly influences the efficiency of Dexter ET. To investigate this, two PAHs with similar chemical structures but distinct planarity, namely **CA** and **BPE**, were selected for comparative analysis (**Figure 5b**). The bowl-shaped **CA** was hypothesized to exhibit lower Dexter ET efficiency than complanate **BPE.** This hypothesis was supported by the temperature-dependent delayed emission spectra (**Figure 5a**). With rising temperature, the **BA@CA** exhibited only a decreased RTP while the **BA@BPE** exhibited an enhanced HTA. The excitation spectrum of **BA@CA** showed a consistent with the absorption spectrum of **CA**, indicating hard electron transfer between BA and CA. Besides, the excitation spectra of **BA@CE** and **BA@BPE** both showed the same characteristic peak at 310 nm, aligning with heated **BA**, demonstrating the thermally released electrons transfer process. To further emphasize the effect of molecular conformation on efficiency, a series of PAHs were chosen as the acceptors to dope into matrix

https://doi.org/10.26434/chemrxiv-2024-vd18g ORCID: https://orcid.org/0000-0002-8679-4491 Content not peer-reviewed by ChemRxiv. License: CC BY-NC-ND 4.0

(**Figure S15**). Their emission results were summarized in **Table S5**. Only plane PAHs exhibited the tunable HTA, whereas the twisted PAHs did not, demonstrating the importance of molecular planarity for Dexter ET. The concentration of **CE** in **BA@CE** system was furtherly increased to generate aggregates, **BA@CE** demonstrated a red-shifted dual emission, featuring green delayed fluorescence peaking at 530 nm and red phosphorescence at 610 nm (**Figures 5a (iii) and S7a**). The fluorescence peak at 530 nm were consistent with that of **CE** solid powder, while the phosphorescence peak at 610 nm matched the emission observed for **CE** powder at 77K (**Figure S8**). Regrettably, the high concentration doping in the system resulted in a degradation of HTA performance. The lifetime of the dual emissions was summarized in **Table S4** and the CIE coordinates were presented in **Figure S7b**. The packing behaviors of aggregates were supposed to influence the electron transfer process. Thus, a convenient regulation strategy for HTA is proposed by combining thermally released electrons and Dexter ET.

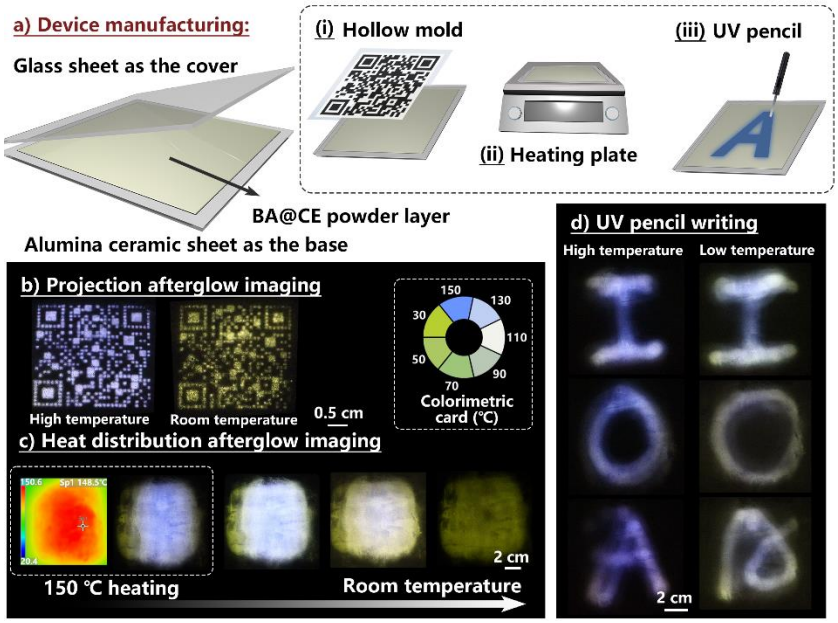

Figure 6. Applications of materials. (a) Fabrication of multifunctional display device; (b) Afterglow images of a two-dimensional code produced by transmitting 365 nm UV light through a hollow mold; (c) Heat distribution mapping via afterglow imaging equipment positioned on the heating platform, where

https://doi.org/10.26434/chemrxiv-2024-vd18g ORCID: https://orcid.org/0000-0002-8679-4491 Content not peer-reviewed by ChemRxiv. License: CC BY-NC-ND 4.0

blue indicates areas of higher temperature and yellow signifies lower temperature regions; (d) Afterglow images of characters written with a 365 nm UV pencil.

The applications of HTA materials. The controllable luminescent attributes of **BA@CE** facilitate the advancement of photonic technologies. Herein, the **BA@CE** is used as the luminescent layer in fabricating a multifunctional display device, enclosed with a transparent glass sheet as the cover and an alumina ceramic sheet serving as the base (**Figure 6a**). Initially, a hollow mold embedding a QR code is utilized in segment (i) for light-printing to produce discernible information within the resulting afterglow images. This afterglow printing demonstrates self-erasing and persistent information storage (**Figure 6b**). Segment (ii) showcases extensive thermal imaging capabilities. The smart photonic device was place on a heating plate and subjected to 150°C for 60 seconds. The afterglow images visualization highlights the blue regions indicating high temperatures, aligned with the focal points of heat concentration (**Figure 6c**). Upon natural cooling to ambient temperature, the afterglow of the heat center gradually changes to white or even yellow, highlighting an efficacious thermal field mapping function. Real-time temperature can be read out through a colorimetric card. In Figure 6d, alphabets “I”, “O”, and “A” were written with 365 nm UV pencil, harnessing the ultralong afterglow of **BA@CE**. UV light writing was seen as a potential application scenario that can temporarily retain handwritten input information, which can be employed as a time-informed information transmit technology.

Conclusion

In summary, we have successfully developed a series of doped materials capable of tunable high-temperature afterglow. This was achieved by utilizing **BA** as the matrix and PAHs as dopant, followed by a thermal dehydration process. The thermal dehydration treatment led to the creation of oxygen vacancies within the matrix, effectively stabilizing the long-lived trapped electrons upon exposure to light. Subsequent thermally release of the trapped electrons and Dexter ET to the dopant facilitated the generation of HTA through electron-hole recombination within the dopant. Therefore, a tunable dual emission was demonstrated by integrating thermally activated HTA with thermally quenched RTP.

https://doi.org/10.26434/chemrxiv-2024-vd18g **ORCID:** https://orcid.org/0000-0002-8679-4491 Content not peer-reviewed by ChemRxiv. **License:** CC BY-NC-ND 4.0

Moreover, comparative analyses with contrast agents **CA** and **BPE** were conducted to explore the Dexter ET mechanism, which indicates that the planarity of dopants is a critical factor in the electron transfer process. This study presents an efficient and universal strategy for fabricating tunable HTA materials by recombination of thermally released electrons.

Methods

Materials. **BA** was purchased from Admas with further purities by recrystallizations. **PHAs** were all obtained from commercial purchase. All solvents were obtained commercially and used as supplied without further purification.

General Methods. The UV-Vis absorption spectra were obtained on a SHIMADZU 2600 spectrophotometer. Delayed emission spectra and emission decay curves were recorded on an Agilent Cary Eclipse spectrophotometer. PL spectra and time-decay curves at 77 K were recorded on EDINBURGH FLS-1000. Thermogravimetric analysis spectra were determined with TGA-50 Thermogravimetric Analyzers (SHIMADZU, Japan). Fourier transform infrared spectroscopy (FT-IR) was obtained on INVENIO S. X-ray diffraction experiments were carried out on D/max2550VB/PC. X-ray photoelectron spectroscopy (XPS) was obtained on ESCALAB 250Xi. Density functional theory (DFT) and time-dependent (TD) DFT calculations were performed with the Gaussian 09 (Revision E.01) software package

Contributions

P. Jiang, B. Ding, X. Ma, and H. Tian conceived the project, P. Jiang designed the molecules and conducted the experiment. P. Jiang, B. Ding, and X. Ma wrote the manuscript. J. Yao, L. Zhou, Z. He, Z. Huang, and C. Yin discussed the results and commented on the manuscript.

Acknowledgements

We gratefully acknowledge the National Key Research and Development Program of China (2022YFB3203500), National Natural Science Foundation of China (22125803, 22020102006, and

https://doi.org/10.26434/chemrxiv-2024-vd18g **ORCID:** https://orcid.org/0000-0002-8679-4491 Content not peer-reviewed by ChemRxiv. **License:** CC BY-NC-ND 4.0

22205062), major projects supported by the Guangxi department of science and technology (AA23062016), and Fundamental Research Funds for the Central Universities.

Ethics declarations

The authors declare no competing interests.

References

[1] Wang, X., and Pu, K. (2023). Molecular substrates for the construction of afterglow imaging probes in disease diagnosis and treatment. Chem. Soc. Rev. 52, 4549-4566. https://doi.org/10.1039/D3CS00006K

[2] Chen, W., Zhang, Y., Li, Q., Jiang, Y., Zhou, H., Liu, Y., Miao, Q., and Gao, M. (2022). Near-Infrared Afterglow Luminescence of Chlorin Nanoparticles for Ultrasensitive In Vivo Imaging. J. Am. Chem. Soc. 144, 6719-6726. https://doi.org/10.1021/jacs.1c10168

[3] Wu, S., Li, Y., Ding, W., Xu, L., Ma, Y., and Zhang, L. (2020). Recent Advances of Persistent Luminescence Nanoparticles in Bioapplications. Nano-micro Lett. 12, 70. https://doi.org/10.1007/s40820-020-0404-8

[4] Yin, G., Huo, G., Qi, M., Liu, D., Li, L., Zhou, J., Le, X., Wang, Y., and Chen, T. (2023). Precisely Coordination-Modulated Ultralong Organic Phosphorescence Enables Biomimetic Fluorescence-Afterglow Dual-Modal Information Encryption. Adv. Funct. Mater. 2023, 2310043. https://doi.org/10.1002/adfm.202310043

[5] Liang, Y., Xu, C., Zhang, H., Wu, S., Li, J.A., Yang, Y., Mao, Z., Luo, S., Liu, C., Shi, G., *et al*. (2023). Color-Tunable Dual-Mode Organic Afterglow from Classical Aggregation-Caused Quenching Compounds for White-Light-Manipulated Anti-Counterfeiting. Angew. Chem. Int. Ed. 62, e202217616. https://doi.org/10.1002/anie.202217616

[6] Zhang, X., Chong, K.C., Xie, Z., and Liu, B. (2023). Color-Tunable Dual-Mode Organic Afterglow for White-Light Emission and Information Encryption Based on Carbazole Doping. Angew. Chem. Int. Ed. 62, e202310335. https://doi.org/10.1002/anie.202310335

[7] Yang, Y., Liang, Y., Zheng, Y., Li, J.A., Wu, S., Zhang, H., Huang, T., Luo, S., Liu, C., Shi, G., *et al*. (2022). Efficient and Color-Tunable Dual-Mode Afterglow from Large-Area and Flexible Polymer-Based Transparent Films for Anti-Counterfeiting and Information Encryption. Angew. Chem. Int. Ed. 61, e202201820. https://doi.org/10.1002/anie.202201820

[8] Yang, X., Waterhouse, G.I.N., Lu, S., and Yu, J. (2023). Recent advances in the design of afterglow materials: mechanisms, structural regulation strategies and applications. Chem. Soc. Rev. 52, 8005-8058. https://doi.org/10.1039/D2CS00993E

[9] Cui, G., Yang, X., Zhang, Y., Fan, Y., Chen, P., Cui, H., Liu, Y., Shi, X., Shang, Q., and Tang, B. (2019). Round-the-Clock Photocatalytic Hydrogen Production with High Efficiency by a Long-Afterglow Material. Angew. Chem. Int. Ed. 58, 1340-1344. https://doi.org/10.1002/anie.201810544

[10] Kim, S.J., Choi, M., Hong, G., and Hahn, S.K. (2022). Controlled afterglow luminescent particles for photochemical tissue bonding. Light. Sci. Appl. 11, 314. https://doi.org/10.1038/s41377-022-01011-3

[11] Zeng, W., and Ye, D. (2023). Seeing cancer via sonoafterglow. Nat. Biomed. Eng. 7, 197-198. https://doi.org/10.1038/s41551-022-00985-0

[12] Xu, C., and Pu, K. (2024). Illuminating cancer with sonoafterglow. Nat. Photonics 18, 301-302. https://doi.org/10.1038/s41566-024-01406-1

https://doi.org/10.26434/chemrxiv-2024-vd18g **ORCID:** https://orcid.org/0000-0002-8679-4491 Content not peer-reviewed by ChemRxiv. **License:** CC BY-NC-ND 4.0

[13] Pham, T.C., Nguyen, V.N., Choi, Y., Lee, S., and Yoon, J. (2021). Recent Strategies to Develop Innovative Photosensitizers for Enhanced Photodynamic Therapy. Chem. Rev. 121, 13454-13619. https://doi.org/10.1021/acs.chemrev.1c00381

[14] Li, D., Yang, Y., Yang, J., Fang, M., Tang, B.Z., and Li, Z. (2022). Completely aqueous processable stimulus responsive organic room temperature phosphorescence materials with tunable afterglow color. Nat. Commun. 13, 347. https://doi.org/10.1038/s41467-022-28011-6

[15] An, Z., Zheng, C., Tao, Y., Chen, R., Shi, H., Chen, T., Wang, Z., Li, H., Deng, R., Liu, X., *et al*. (2015). Stabilizing triplet excited states for ultralong organic phosphorescence. Nat. Mater. 14, 685-690. https://doi.org/10.1038/nmat4259

[16] Gu, L., Shi, H., Bian, L., Gu, M., Ling, K., Wang, X., Ma, H., Cai, S., Ning, W., Fu, L., *et al*. (2019). Colour-tunable ultra-long organic phosphorescence of a single-component molecular crystal. Nat. Photonics 13, 406-411. https://doi.org/10.1038/s41566-019-0408-4

[17] Li, S., Fu, L., Xiao, X., Geng, H., Liao, Q., Liao, Y., and Fu, H. (2021). Regulation of Thermally Activated Delayed Fluorescence to Room-Temperature Phosphorescent Emission Channels by Controlling the Excited-States Dynamics via J- and H-Aggregation. Angew. Chem. Int. Ed. 60, 18059-18064. https://doi.org/10.1002/anie.202103192

[18] Chen, K., Jiang, Y., Zhu, Y., Lei, Y., Dai, W., Liu, M., Cai, Z., Wu, H., Huang, X., and Dong, Y. (2022). Host to regulate the T_1-S_1 and T_1–S_0 processes of guest excitons in doped systems to control the TADF and RTP emissions. J. Mater. Chem. C 10, 11607-11613. https://doi.org/10.1039/D2TC02167F

[19] Ding, B.B., Ma, L.W., Huang, Z.Z., Ma, X., Tian, H. (2021). Engendering persistent organic room temperature phosphorescence by trace ingredient incorporation. Sci. Adv. 7, eabf9668. https://doi.org/10.1126/sciadv.abf9668

[20] Zhao, Y., Ding, B., Huang, Z., and Ma, X. (2022). Highly efficient organic long persistent luminescence based on host-guest doping systems. Chem. Sci. 13, 8412-8416. https://doi.org/10.1039/D2SC01622B

[21] Xie, Z., Zhang, X., Wang, H., Huang, C., Sun, H., Dong, M., Ji, L., An, Z., Yu, T., and Huang, W. (2021). Wide-range lifetime-tunable and responsive ultralong organic phosphorescent multi-host/guest system. Nat. Commun. 12, 3522. https://doi.org/10.1038/s41467-021-23742-4

[22] Chen, B., Huang, W., and Zhang, G. (2023). Observation of Chiral-selective room-temperature phosphorescence enhancement via chirality-dependent energy transfer. Nat Commun 14, 1514. https://doi.org/10.1038/s41467-023-37157-w

[23] Ding, B., Ma, X., and Tian, H. (2023). Recent Advances of Pure Organic Room Temperature Phosphorescence Based on Functional Polymers. Acc. Mater. Res. 4, 827-838. https://doi.org/10.1021/accountsmr.3c00090

[24] Huang, J., Wang, X., Wang, G., Li, J., Deng, X., Chen, X., Xu, Y., Lei, C., and Zhang, K. (2022). Polymer-Based TADF-Type Organic Afterglow. J. Phy. Chem. C 126, 20728-20738. https://doi.org/10.1021/acs.jpcc.2c07499

[25] Huang, Z.Z., He, Z.Y., Ding, B.B., Tian, H., and Ma, X. (2022). Photoprogrammable circularly polarized phosphorescence switching of chiral helical polyacetylene thin films. Nat. Commun. 13, 7841. https://doi.org/10.1038/s41467-022-35625-3

[26] Zhou, L., Song, J., He, Z., Liu, Y., Jiang, P., Li, T., and Ma, X. (2024). Achieving Efficient Dark Blue Room-Temperature Phosphorescence with Ultra-Wide Range Tunable-Lifetime. Angew. Chem. Int. Ed. 63, e202403773. https://doi.org/10.1002/anie.202403773

[27] Gao, J., Wu, X., Jiang, X., Li, M., He, R., and Shen, W. (2023). Achieving purple light excitable high-efficiency temperature-responsive dual- and single-mode afterglow in carbon dots. Carbon 208, 365-373. https://doi.org/10.1016/j.carbon.2023.03.048

[28] Meng, S., Cheng, D., Gu, H., Li, Y., Qin, Y., Tan, J., and Li, Q. (2023). Mechanical Force-Induced Color-Variable Luminescence of Carbon Dots in Boric Acid Matrix. Molecules 28, 3388. https://doi.org/10.3390/molecules28083388

https://doi.org/10.26434/chemrxiv-2024-vd18g **ORCID:** https://orcid.org/0000-0002-8679-4491 Content not peer-reviewed by ChemRxiv. **License:** CC BY-NC-ND 4.0

[29] Sun, Y., Liu, J., Pang, X., Zhang, X., Zhuang, J., Zhang, H., Hu, C., Zheng, M., Lei, B., and Liu, Y. (2020). Temperature-responsive conversion of thermally activated delayed fluorescence and room-temperature phosphorescence of carbon dots in silica. J. Mater. Chem.C 8, 5744-5751. https://doi.org/10.1039/D0TC00507J

[30] Wang, B., and Lu, S. (2022). The light of carbon dots: From mechanism to applications. Matter 5, 110-149. https://doi.org/10.1016/j.matt.2021.10.016

[31] Tan, S., Jinnai, K., Kabe, R., and Adachi, C. (2021). Long-Persistent Luminescence from an Exciplex-Based Organic Light-Emitting Diode. Adv. Mater. 33, e2008844. https://doi.org/10.1002/adma.202008844

[32] Sk, B., and Hirata, S. (2024). Symmetry-Breaking Triplet Excited State Enhances Red Afterglow Enabling Ubiquitous Afterglow Readout. Adv. Sci. 11, e2308897. https://doi.org/10.1002/advs.202308897

[33] Wang, Y., Li, Q., Qu, L., Huang, J., Zhu, Y., Li, C., Chen, Q., Zheng, Y., and Yang, C. (2024). Effective Long Afterglow Amplification Induced by Surface Coordination Interaction. Adv. Sci. 11, e2306942. https://doi.org/10.1002/advs.202306942

[34] Man, Z., Lv, Z., Xu, Z., Liu, M., He, J., Liao, Q., Yao, J., Peng, Q., and Fu, H. (2022). Excitation-Wavelength-Dependent Organic Long-Persistent Luminescence Originating from Excited-State Long-Range Proton Transfer. J. Am. Chem. Soc. 144, 12652-12660. https://doi.org/10.1021/jacs.2c01248

[35] Zhu, T., Yang, T., Zhang, Q., and Yuan, W.Z. (2022). Clustering and halogen effects enabled red/near-infrared room temperature phosphorescence from aliphatic cyclic imides. Nat. Commun. 13, 2658. https://doi.org/10.1038/s41467-022-30368-7

[36] Li, Z., Cao, S., Zheng, Y., Song, L., Zhang, H., and Zhao, Y. (2023). Colorful Ultralong Room Temperature Phosphorescent Afterglow with Excitation Wavelength Dependence Based on Boric Acid Matrix. Adv. Funct. Mater. 34, 2306956. https://doi.org/10.1002/adfm.202306956

[37] Zhou, B., Xiao, G., and Yan, D. (2021). Boosting Wide-Range Tunable Long-Afterglow in 1D Metal-Organic Halide Micro/Nanocrystals for Space/Time-Resolved Information Photonics. Adv. Mater. 33, e2007571. https://doi.org/10.1002/adma.202007571

[38] Pan, Y., Li, J., Wang, X., Sun, Y., Li, J., Wang, B., and Zhang, K. (2021). Highly Efficient TADF-Type Organic Afterglow of Long Emission Wavelengths. Adv. Funct. Mater. 32, 2110207. https://doi.org/10.1002/adfm.202110207

[39] Shen, S., Sun, Y., Wang, D., Zhang, Z., Shi, Y.E., and Wang, Z. (2022). Efficient blue TADF-type organic afterglow material via boric acid-assisted confinement. Chem. Commun. 58, 11418-11421. https://doi.org/10.1039/D2CC04544C

[40] Wang, L., Tu, D., Li, C., Han, S., Wen, F., Yu, S., Yi, X., Xie, Z., and Chen, X. (2023). Engineering trap distribution to achieve multicolor persistent and photostimulated luminescence from ultraviolet to near-infrared II. Matter 6, 4261-4273. https://doi.org/10.1016/j.matt.2023.09.016

[41] Wu, M., Li, J., Huang, J., Wang, X., Wang, G., Chen, X., Li, X., Chen, X., Ding, S., Zhang, H., *et al.* (2023). The unexpected mechanism of transformation from conventional room-temperature phosphorescence to TADF-type organic afterglow triggered by simple chemical modification. J. Mater. Chem. C 11, 2291-2301. https://doi.org/10.1039/D2TC05261J

[42] Zheng, X., Huang, Y., Lv, W., Fan, J., Ling, Q., and Lin, Z. (2022). Nearly Unity Quantum Yield Persistent Room-Temperature Phosphorescence from Heavy Atom-Free Rigid Inorganic/Organic Hybrid Frameworks. Angew. Chem. Int. Ed. 61, e202207104. https://doi.org/10.1002/anie.202207104

[43] Zhou, B., Qi, Z., Dai, M., Xing, C., and Yan, D. (2023). Ultralow-loss Optical Waveguides through Balancing Deep-Blue TADF and Orange Room Temperature Phosphorescence in Hybrid Antimony Halide Microstructures. Angew. Chem. Int. Ed. 62, e202309913. https://doi.org/10.1002/anie.202309913

[44] Zhao, W., He, Z., and Tang, B.Z. (2020). Room-temperature phosphorescence from organic aggregates. Nat. Rev. Mater. 5, 869-885. https://doi.org/10.1038/s41578-020-0223-z

https://doi.org/10.26434/chemrxiv-2024-vd18g **ORCID:** https://orcid.org/0000-0002-8679-4491 Content not peer-reviewed by ChemRxiv. **License:** CC BY-NC-ND 4.0

[45] Jiang, P., Liu, Y.W., Ding, B.B., and Ma, X. (2024). Regulation Strategies of Dynamic Organic Room-Temperature Phosphorescence Materials. Chem. Bio. Eng. 1, 13-25. https://doi.org/10.1021/cbe.3c00095

[46] Zhao, W., He, Z., Lam, Jacky W.Y., Peng, Q., Ma, H., Shuai, Z., Bai, G., Hao, J., and Tang, Ben Z. (2016). Rational Molecular Design for Achieving Persistent and Efficient Pure Organic Room-Temperature Phosphorescence. Chem 1, 592-602. http://dx.doi.org/10.1016/j.chempr.2016.08.010

[47] Lin, C., Wu, Z., Ma, H., Liu, J., You, S., Lv, A., Ye, W., Xu, J., Shi, H., Zha, B., *et al*. (2024). Charge trapping for controllable persistent luminescence in organics. Nat. Photonics 18, 350-356. https://doi.org/10.1038/s41566-024-01396-0

[48] Brocklehurst, B., Russell, R. (1967). Thermoluminescence from Recombination of Organic Ions. Nature 213, 65. https://doi.org/10.1038/213065a0

[49] King, G.E., Guralnik, B., Valla, P.G., and Herman, F. (2016). Trapped-charge thermochronometry and thermometry: A status review. Chem. Geol. 446, 3-17. https://doi.org/10.1016/j.chemgeo.2016.08.023

[50] Stagi, L., Malfatti, L., Zollo, A., Livraghi, S., Carboni, D., Chiriu, D., Corpino, R., Ricci, P.C., Cappai, A., Carbonaro, C.M., *et al.* (2023). Phosphorescence by Trapping Defects in Boric Acid Induced by Thermal Processing. Adv. Optical Mater. 12, 2302682. https://doi.org/10.1002/adom.202302682

[51] Zhou, Z., Jiang, K., Chen, N., Xie, Z., Lei, B., Zhuang, J., Zhang, X., Liu, Y., and Hu, C. (2020). Room temperature long afterglow from boron oxide: A boric acid calcined product. Mater. Lett. 276, 128226. https://doi.org/10.1016/j.matlet.2020.128226

[52] Xiao, F., Gao, H., Lei, Y., Dai, W., Liu, M., Zheng, X., Cai, Z., Huang, X., Wu, H., and Ding, D. (2022). Guest-host doped strategy for constructing ultralong-lifetime near-infrared organic phosphorescence materials for bioimaging. Nat. Commun. 13, 186. https://doi.org/10.1038/s41467-021-27914-0

[53] Khampuanbut, A., Santalelat, S., Pankiew, A., Channei, D., Pornsuwan, S., Faungnawakij, K., Phanichphant, S., and Inceesungvorn, B. (2020). Visible-light-driven WO(3)/BiOBr heterojunction photocatalysts for oxidative coupling of amines to imines: Energy band alignment and mechanistic insight. J. Colloid Interface Sci. 560, 213-224. https://doi.org/10.1016/j.jcis.2019.10.057

[54] Kabe, R., and Adachi, C. (2017). Organic long persistent luminescence. Nature 550, 384-387. https://doi.org/10.1038/nature24010

[55] Li, F., Gillett, A.J., Gu, Q., Ding, J., Chen, Z., Hele, T.J.H., Myers, W.K., Friend, R.H., and Evans, E.W. (2022). Singlet and triplet to doublet energy transfer: improving organic light-emitting diodes with radicals. Nat. Commun. 13, 2744. https://doi.org/10.1038/s41467-022-29759-7

[56] Alam, P., Leung, N.L.C., Liu, J., Cheung, T.S., Zhang, X., He, Z., Kwok, R.T.K., Lam, J.W.Y., Sung, H.H.Y., Williams, I.D., *et al*. (2020). Two Are Better Than One: A Design Principle for Ultralong-Persistent Luminescence of Pure Organics. Adv. Mater. 32, e2001026. https://doi.org/10.1002/adma.202001026

https://doi.org/10.26434/chemrxiv-2024-vd18g **ORCID:** https://orcid.org/0000-0002-8679-4491 Content not peer-reviewed by ChemRxiv. **License:** CC BY-NC-ND 4.0